

Model for estimating the penetration depth limit of the time-reversed ultrasonically encoded optical focusing technique

Mooseok Jang,^{*} Haowen Ruan, Benjamin Judkewitz, and Changhuei Yang

Electrical Engineering, California Institute of Technology, 1200 E California Boulevard, Pasadena, California 91125, USA

^{*}mjang@caltech.edu

Abstract: The time-reversed ultrasonically encoded (TRUE) optical focusing technique is a method that is capable of focusing light deep within a scattering medium. This theoretical study aims to explore the depth limits of the TRUE technique for biological tissues in the context of two primary constraints – the safety limit of the incident light fluence and a limited TRUE’s recording time (assumed to be 1 ms), as dynamic scatterer movements in a living sample can break the time-reversal scattering symmetry. Our numerical simulation indicates that TRUE has the potential to render an optical focus with a peak-to-background ratio of ~ 2 at a depth of ~ 103 mm at wavelength of 800 nm in a phantom with tissue scattering characteristics. This study sheds light on the allocation of photon budget in each step of the TRUE technique, the impact of low signal on the phase measurement error, and the eventual impact of the phase measurement error on the strength of the TRUE optical focus.

©2014 Optical Society of America

OCIS codes: (070.5040) Phase conjugation; (090.1995) Digital holography; (090.2880) Holographic interferometry; (110.7050) Turbid media; (170.7170) Ultrasound; (220.1080) Active or adaptive optics.

References and links

1. V. Ntziachristos, “Going deeper than microscopy: the optical imaging frontier in biology,” *Nat. Methods* **7**(8), 603–614 (2010).
2. X. Xu, H. Liu, and L. V. Wang, “Time-reversed ultrasonically encoded optical focusing into scattering media,” *Nat. Photonics* **5**(3), 154–157 (2011).
3. Y. M. Wang, B. Judkewitz, C. A. Dimarzio, and C. Yang, “Deep-tissue focal fluorescence imaging with digitally time-reversed ultrasound-encoded light,” *Nat Commun* **3**, 928 (2012).
4. K. Si, R. Fiolka, and M. Cui, “Fluorescence imaging beyond the ballistic regime by ultrasound pulse guided digital phase conjugation,” *Nat. Photonics* **6**(10), 657–661 (2012).
5. K. Si, R. Fiolka, and M. Cui, “Breaking the spatial resolution barrier via iterative sound-light interaction in deep tissue microscopy,” *Sci. Rep.* **2**, 748 (2012).
6. L. V. Wang, “Mechanisms of Ultrasonic Modulation of Multiply Scattered Coherent Light: An Analytic Model,” *Phys. Rev. Lett.* **87**(4), 043903 (2001).
7. Z. Yaqoob, D. Psaltis, M. S. Feld, and C. Yang, “Optical Phase Conjugation for Turbidity Suppression in Biological Samples,” *Nat. Photonics* **2**(2), 110–115 (2008).
8. M. Cui, E. J. McDowell, and C. Yang, “An in vivo study of turbidity suppression by optical phase conjugation (TSOPC) on rabbit ear,” *Opt. Express* **18**(1), 25–30 (2010).
9. M. Cui and C. Yang, “Implementation of a digital optical phase conjugation system and its application to study the robustness of turbidity suppression by phase conjugation,” *Opt. Express* **18**(4), 3444–3455 (2010).
10. B. Judkewitz, Y. M. Wang, R. Horstmeyer, A. Mathy, and C. Yang, “Speckle-scale focusing in the diffusive regime with time-reversal of variance-encoded light (TROVE),” *Nat. Photonics* **7**(4), 300–305 (2013).
11. Laser Institute of America, *American National Standard for Safe Use of Lasers ANSI Z136.1–2000* (American National Standards Institute Inc., 2000).
12. I. Vellekoop and C. Aegerter, “Focusing light through living tissue,” *Proc. SPIE* **7554**, 755430 (2010).
13. D. B. Conkey, A. M. Caravaca-Aguirre, and R. Piestun, “High-speed scattering medium characterization with application to focusing light through turbid media,” *Opt. Express* **20**(2), 1733–1740 (2012).
14. I. Yamaguchi and T. Zhang, “Phase-shifting digital holography,” *Opt. Lett.* **27**, 1108–1110 (1997).

15. G. Marquez, L. V. Wang, S. P. Lin, J. A. Schwartz, and S. L. Thomsen, "Anisotropy in the absorption and scattering spectra of chicken breast tissue," *Appl. Opt.* **37**(4), 798–804 (1998).
16. D. Dalecki, "Mechanical bioeffects of ultrasound," *Annu. Rev. Biomed. Eng.* **6**(1), 229–248 (2004).
17. U.S. Department of Health and Human Services, "Guidance for Industry and FDA Staff—Information for Manufacturers Seeking Marketing Clearance of Diagnostic Ultrasound Systems and Transducers," (2008).
18. M. Cui, E. J. McDowell, and C. Yang, "An in vivo study of turbidity suppression by optical phase conjugation (TSOPC) on rabbit ear," *Opt. Express* **18**(1), 25–30 (2010).
19. J. Goodman, *Speckle Phenomena in Optics: Theory and Applications* (Roberts and Company Publishers, 2007).
20. S. M. Popoff, G. Lerosey, R. Carminati, M. Fink, A. C. Boccara, and S. Gigan, "Measuring the Transmission Matrix in Optics: An Approach to the Study and Control of Light Propagation in Disordered Media," *Phys. Rev. Lett.* **104**(10), 100601 (2010).
21. A. Mosk, A. Lagendijk, G. Lerosey, and M. Fink, "Controlling waves in space and time for imaging and focusing in complex media," *Nat. Photonics* **6**(5), 283–292 (2012).
22. F. Martelli, S. Del Bianco, A. Ismaelli, and G. Zaccanti, *Light Propagation through Biological Tissue and Other Diffusive Media: Theory, Solutions, and Software* (SPIE Press, 2010).
23. R. C. Haskell, L. O. Svaasand, T. T. Tsay, T. C. Feng, M. S. McAdams, and B. J. Tromberg, "Boundary conditions for the diffusion equation in radiative transfer," *J. Opt. Soc. Am. A* **11**(10), 2727–2741 (1994).
24. W. Riley and W. Klein, "Piezo Optic Coefficients of Liquids," *J. Acoust. Soc. Am.* **42**(6), 1258–1261 (1967).
25. M. Moharam, T. Gaylord, and R. Magnusson, "Criteria for Raman-Nath regime diffraction by phase gratings," *Opt. Commun.* **32**(1), 19–23 (1980).
26. T. K. Gaylord and M. G. Moharam, "Thin and thick gratings: terminology clarification," *Appl. Opt.* **20**(19), 3271–3273 (1981).
27. J. Huang, J. Nissen, and E. Bodegom, "Diffraction of light by a focused ultrasonic wave," *J. Appl. Phys.* **71**(1), 70–75 (1992).
28. I. M. Vellekoop and A. P. Mosk, "Focusing coherent light through opaque strongly scattering media," *Opt. Lett.* **32**(16), 2309–2311 (2007).
29. M. O. Culjat, D. Goldenberg, P. Tewari, and R. S. Singh, "A review of tissue substitutes for ultrasound imaging," *Ultrasound Med. Biol.* **36**(6), 861–873 (2010).

1. Introduction

Because biological tissues are optically turbid, biomedical optical techniques have very limited penetration depth. The depth limit is essentially given by the characteristic length at which photons lose their directionality (one transport mean free path). Although it depends on the type of tissue and the light wavelength, this accessible depth is typically around one millimeter [1] or less. Thus, when used noninvasively, the utility of optical techniques in research and diagnosis has long been restricted to the superficial layers of tissue.

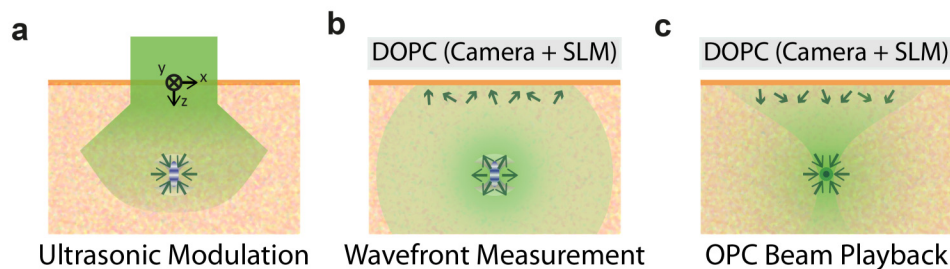


Fig. 1. Schematic of the TRUE focusing principle with digital optical phase conjugation system (DOPC). (a) Collimated incident beam propagates through scattering medium. Light component passing through the ultrasound focus is encoded with ultrasound frequency. (b) Ultrasound-modulated light propagates back to the tissue surface. The distorted wave front is measured by a sensor in the DOPC system. (c) Spatial light modulator (SLM) reproduces a phase-conjugated copy of the measured wave front. The OPC beam with time-reversal characteristic is focused back into the US spot.

During the past few years, there has been considerable effort to break this limit by the technique of time reversal of ultrasonically encoded light, which combines ultrasonic light modulation with optical phase conjugation (OPC) [2–5]. OPC is an optical process by which an incoming wavefront is reproduced and propagated back so that the phase-conjugated light wave can retrace the original light wave in the backward direction (time-reversal property). In

TRUE, the ultrasound is focused deep inside a tissue sample, while the tissue is illuminated by a laser beam. Diffuse laser light reaching the US focus is then frequency-shifted by the acousto-optic effect [6], which serves as a “tag”. Tagged US frequency-shifted light leaving the sample is selectively detected and phase-conjugated. Due to the time-reversal symmetry of light propagation, phase-conjugated light in turn propagates back to the ultrasound focus, where it creates an optical focus.

Recently, TRUE has been experimentally achieved by both analog and digital OPC systems. Analog method utilizes nonlinear optical phenomena such as Brillouin scattering and nonlinear susceptibility of photorefractive medium [2,7,8], on the other hand, the digital method (DOPC) is implemented with digital devices - wavefront sensor and spatial light modulator (SLM) [3–5,9,10]. The principle of DOPC-based TRUE focusing technique is described in Fig. 1. The demonstration of deep-tissue light focusing with DOPC has been made with a resolution of $\sim 40\ \mu\text{m}$ at a depth of 2.5 mm inside biological tissue [3].

In principle, with perfect wavefront measurements, the TRUE technique could create an optical focus even tens of centimeters deep in the human body. However, there are two important constraints that fundamentally limit the penetration depth of TRUE focusing technique for living tissue applications. First, the incident light fluence per pulse at the tissue surface has to be smaller than the tissue damage threshold ($20\ \text{mJ cm}^{-2}$ according to the ANSI medical safety standard [11]). We note that a pulsed light source is assumed as it yields more photons under the safety standard. Second, wavefront measurement and OPC playback (in Fig. 1) should be performed within a short time-window, before the movement of scatters significantly changes the tissue (as an optical object), thereby destroying the time-reversal symmetry. This sample-dependent time-window, which is also called the decorrelation time (t_{dec}), depends on the sample stability and depth. For most living tissues, it ranges from several milliseconds to seconds [8,12,13]. In our analysis, we will consider a TRUE recording time of period $t_{\text{rec}} = 1\ \text{ms}$. We assume this time to be significantly shorter than t_{dec} . In the event that a shorter t_{dec} requires a shorter t_{rec} , the analysis in this study can be rescaled in a straightforward fashion, as the total signal photon budget is simply proportional to t_{rec} .

These two restrictions (one on incident light intensity and the other one on wavefront recording time) limit the incident photon number and, in turn, the number of frequency-shifted photons that can be collected at the surface for the wavefront measurement. As the signal level decreases with increasing tissue depth, shot-noise deteriorates the validity of the wavefront measurement and, in turn, the contrast and intensity of the TRUE focus.

In this study, we developed a numerical model to calculate the penetration depth limit of the TRUE technique given by the abovementioned constraints in living tissue applications. Our analysis is not meant to be exhaustive. One of its purposes is to establish a basic model system for understanding the interplay between various optical and ultrasonic parameters in determining the useful focusing depth of TRUE. A reader interested in a particular optical geometry, more sophisticated modeling assumptions, or a specific set of constraints can adapt our model for his/her respective purpose.

Additionally, this paper is aimed at elucidating the fundamental optical limitations of TRUE focusing technique given by shot noise at low signal level, rather than focusing on limitations associated with current technical hurdles. For this purpose, we specifically modeled TRUE system implemented with digital version of OPC system with idealized fidelity. The idealized assumptions used here are listed in Section 2.2; we also compare the current technical limits to these assumptions in that section. We note that modification would need to be made on our model if the reader desires to investigate the effect of shot noise on analog OPC system as those systems exploit nonlinear optical phenomena to achieve their effects. There are likely more restrictive constraints that would have to be considered in that scenario.

The numerical simulation of TRUE developed here consists of the following steps, which are detailed in the Methods section: First, we simulate light propagation from the tissue surface (at the safety limit and within t_{rec}) to the deep-tissue US focus with diffusion approximation. Second, the amount of US frequency-shifted light is determined using the Raman-Nath theory. Third, the intensity of frequency-shifted light propagating back to the surface is determined and used to calculate the detection shot-noise. Finally, we determine the relationship between shot-noise and focus contrast (peak-to-background ratio, PBR) and determine that the practical depth limit of DOPC is in the range of 30–100 mm with the parameters in our consideration. We expect that our model will provide a framework to check the feasibility and performance of potential applications of the TRUE technique.

This paper is structured as follows. The next two sections describe the model geometry and assumptions used are described in detail. The following sections will provide details of the methods with a flow chart. We will then present the numerical result regarding the dependence of the photon budget and PBR on the target depths. Finally, we will determine the fundamental depth limit from the result and discuss the utility of our model.

2. Methods

2.1 Model geometry description

Due to its relevance for biomedical imaging, a backscattering geometry is considered in this numerical study. The specific physical model geometry we are considering here is shown in Fig. 1. The target sample is a semi-infinite tissue phantom.

We assume that the DOPC system abuts the sample at its interface. For the sake of simplicity, we blackbox the DOPC and simply assume that the system is able to record the wavefront of the backscattered light exiting the interface with high fidelity and is also able to generate a corresponding phase-conjugate wavefront with high fidelity for playback. We assume that the DOPC is able to span $20\text{ cm} \times 20\text{ cm}$ of the interface surface to ensure that most of the ultrasound-modulated light is captured by the DOPC system. The wavefront measurement is assumed to be performed via interferometry where the reference beam's phase is stepped in quadrature [14] as done in previous works [3–5,9,10]. Thus, the wavefront recording time is divided into four sensor exposure periods of 0.25 ms ($=t_{rec}/4$) for each interference pattern. Idealized assumptions will be detailed in Section 2.2.

With regard to the incident light, we assume that the probe light field has a width of $5.1\text{ cm} \times 5.1\text{ cm}$ and fluence per pulse at the ANSI safety limit of 20 mJ cm^{-2} . To perform quadrature interferometry within our specified time window of 1 ms, the pulse repetition rate would have to be 4 kHz. The pulse duration (p_{dur}) does not affect the result as long as it is sufficiently short compared to the ultrasound pulse. The cases at three wavelengths – 532, 633, and 800 nm – are studied. The corresponding sample absorptive attenuation coefficients are 0.038, 0.008, and 0.005 mm^{-1} , and reduced scattering coefficients 0.33, 0.24, and 0.17 mm^{-1} , respectively [15]. In this paper, we mainly present plots of the results for wavelength of 800 nm; of the three wavelengths, 800 nm leads to the greatest penetration depth.

Table 1. Coordinate System and Parameters Used During the Calculation

| | | |
|---|---|--|
| Coordinate system | Cartesian coordinate system is used. The origin is set on the center of the incident light field on the tissue surface. xy-plane is on the tissue surface. And, z-axis is normal to the surface pointing toward the inside of the tissue. | |
| Incident light | Fluence per pulse (uniform) | $= 20 \text{ mJcm}^{-2}$ |
| | Beam width | $= 5.1 \text{ cm} \times 5.1 \text{ cm}$ |
| | Total energy per pulse | $= 0.52 \text{ J}$ $= 2.1 \times 10^{18} \text{ photons}$ |
| | Pulse duration | $= 10 \text{ ns}$ |
| | Light wavelength (λ) | $= 800 \text{ nm}$ |
| Point sources sampling the incident light | Point source spacing | $= 0.2 \text{ mm}$ |
| | Number of point source | $= 676$ |
| | Energy per the point source (E_{point}) | $= 8 \times 10^{-6} \text{ J}$ |
| Ultrasound | Ultrasound frequency | $= 50 \text{ MHz}$ |
| | Ultrasound wavelength (λ_{US}) | $= 30 \mu\text{m}$ |
| | Pressure at the ultrasound focus (P) | $= 2.35 \text{ MPa}$ |
| | Surface area of US spot ($A_{\text{US}} = \pi \lambda_{\text{US}}^2 / 2$) | $\approx 1410 \mu\text{m}^2$ |
| Emerging speckle field | Speckle size ($(\lambda/2)^2$) | $\approx 0.16 \mu\text{m}^2$ |
| | Grid cell spacing (at which emerging photon number is evaluated) | $= 0.1 \text{ mm}$ |
| | Number of modes (speckles) on a grid cell (M_{grid}) | $= 6.25 \times 10^4$ |
| Optical properties of tissue | Reduced scattering coefficient (μ'_s) | $= 0.17 \text{ mm}^{-1}$ |
| | Absorption coefficient (μ_a) | $= 0.005 \text{ mm}^{-1}$ |

With regard to the ultrasound, we assume that a transducer with a numerical aperture of 1 is placed at the same tissue surface. The generated ultrasound focal spot has transverse and longitudinal spot sizes of $15 \mu\text{m}$ and $30 \mu\text{m}$, respectively, and we assume that the ultrasound is also pulsed with a frequency of 4 kHz . The ultrasound frequency is 50 MHz . Each ultrasound pulse (20 ns long, corresponding to a single cycle) is assumed to modulate photons from each light pulse, as the light pulse is not broadened much at the dimension in our consideration. Pressure at the target depth is set as 2.35 MPa corresponding to the safety standard (spatial-peak pulse-average intensity of 190 Wcm^{-2}) [16,17]. The corresponding mechanical index value ($= 0.33$) and spatial-peak temporal-average intensity ($= 15 \text{ mWcm}^{-2}$)

is well below the safety standards ($=1.9$ and 720mWcm^{-2} for the respective standards) [16,17]. Table 1 summarizes the parameters used in our analysis.

2. 2 Assumptions

As previously mentioned, this paper is primarily aimed at elucidating fundamental optical limitations in the TRUE focusing technique, rather than focusing on limitations associated with current technical hurdles. As such, we make idealized assumptions that exceed the currently available performances of sub-systems that make up the TRUE focusing system. This section details these assumptions and compares them with the current technical limit.

Assumption 1. The DOPC sensor and SLM have a sufficiently high number of pixels, and the pixels are sufficiently small to capture the nuances of all the backscattered light field. This assumption ensures that, in the absence of noise, our sensor and SLM are not limiting factors in characterizing the phase of all the optical modes (wave front) of the backscattered light field. In a fully developed speckle field, the total number of optical modes associated with light emerging from a $20\text{cm}\times 20\text{cm}$ surface is given by $\sim 2.5\times 10^{11}$. This is ~ 5 order of magnitude greater than the number of pixels available on a high-end commercial sensor and SLM. We do note that there are no physical laws that prevent the scaling up of pixel counts in these digital components. In practical experiments, it may also be possible to manage the way we select dominant optical modes [10] so that we can usefully devote the available system pixels to optimally collect signals.

Assumption 2. Each sensor pixel has an unlimited well depth and 100% quantum efficiency as well as zero dark noise and readout noise so that our wavefront measurement by interferometry is only subjected to shot noise. In practice, sensor sensitivity suffers from dark noise, readout noise, limited well depth, and quantum efficiency. However, as we are more interested in the fundamental penetration depth limit imposed from Poissonian shot noise at low signal level, this assumption allows us to explore TRUE's depth penetration capability without getting bogged down by the current capabilities of sensors.

Assumption 3. The scatterers are assumed to be static during 1ms ($=t_{\text{rec}}$). In the absence of substantial blood flow, one early experiment indicates that photorefractive crystal-based OPC playback of the wavefront can adequately perform the time-reversal of multiply scattered light at a living tissue thickness of $\sim 7\text{mm}$ with a decorrelation time-scale of one second (wavelength of 532nm , live rabbit ear [18]). Intrinsic cellular motions in a living sample can be expected to set the time-window for TRUE application in living targets. Blood pulsation and unintentional movement of living sample will induce additional bulk movement of scatterers that can deteriorate t_{dec} even further. Appropriate methods for holding the tissue robustly in place would likely be required as the proper physical fixing of tissue (the rabbit ear was gently held between two glass slides) is likely a major reason for why such a long decorrelation time was observed in [8]. The presence of moving blood within the blood vessels also constitutes a signal loss mechanism (light that passes through the blood vessel cannot be time-reversed) that results in a diminished PBR. Thus, we expect that, as long as blood pulsation is minimized and the surrounding tissues are not perturbed by blood flow, photon paths through those unperturbed tissues would still preserve their time-symmetry property.

Assumption 4. Incident probe light is only modulated at the US spot. Here, we assume both probe light and ultrasound are pulsed. Both theoretically and experimentally, we can only modulate a light component passing through the US spot by triggering an ultrasound pulse with a proper delay (which corresponds to the light pulse travel time to the US spot) with respect to light pulse generation [3].

Assumption 5. The backscattered light field has a fully developed speckle pattern where the dimension of speckle granularity (autocorrelation area) is $(\lambda/2)^2$ [19]. This is a valid assumption for the large-depth TRUE focus we are presently considering. By this assumption, the transmission matrix components, which relate the field at US spot and the field at the tissue surface, can be represented mathematically by a complex random Gaussian matrix [20,21].

Assumption 6. Calculation of phase map and its display takes negligible time compared to the wavefront recording time. Because we set our recording time at 1 ms , the exposure time is set to 0.25 ms ($=t_{\text{rec}}/4$) for each interferogram. In a typical TRUE setup, the calculation of the phase map from four interferograms takes around 200 milliseconds, which can be significantly shortened with a better computing unit. Moreover, the display device (liquid-crystal-on-silicon) operates at 60 Hz ($\sim 15\text{ ms}$). We note that there is no physical limitation that prevents TRUE systems from achieving much faster display times. In the event that liquid crystal technology imposes a reaction time that is difficult to tackle, it is possible to envision switching to a MEMS-based display device to circumvent the display reaction time problem.

2.3 Model analysis strategy

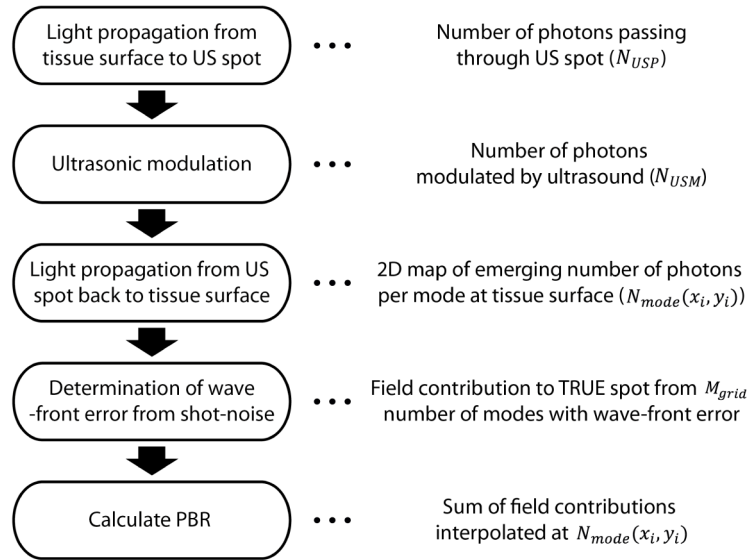


Fig. 2. Flow chart of simulation procedure. 2D photon flux map emerging from the tissue surface is calculated from the first three steps regarding light propagation and ultrasonic light modulation. Then, wavefront measurement error resulting from shot-noise is determined to calculate the field contribution from M_{grid} number of modes to the TRUE focal spot

($A_{\text{OPC_LUT}} e^{i\phi_{\text{OPC_LUT}}}$). In the last step, PBR is calculated by summing up the field contributions from each simulation grid cell. Here, we use the lookup table approach (field contribution is interpolated from) that we will describe in detail at Section 2.3.2 and 2.3.3.

The simulation consists of the following steps (Fig. 2): First, we simulate light propagation from the tissue surface (at the safety limit and within t_{rec}) to the deep-tissue US focus with diffusion approximation to calculate the number of photons passing through the ultrasound spot (N_{USP}). Second, the number of ultrasound-modulated photons (N_{USM}) is calculated by estimating the ultrasound-modulation efficiency with the Raman-Nath theory. Third, by propagating back the ultrasound-tagged photons emanating from the US focus, we mapped

out the emerging tagged photon flux on the 2D tissue surface ($N_{\text{mode}}(x_{l,m}, y_{l,m})$). Detection shot-noise is determined using the 2D photon flux. Finally, we determine the detailed relationship between shot-noise and focus contrast (peak-to-background ratio, PBR_{TRUE}) and determine the practical depth limit of TRUE.

Simply put, PBR_{TRUE} is the ratio of fluence at the TRUE focal spot and the surrounding background. Despite the OPC beam's time-reversal property, background fluence is always expected to be present because the information of the tagged light emerged from US spot is partially lost due to light absorption during its propagation and partial measurement of the emerging wavefront (from one side of the tissue). Approximately speaking, it is proportional to the effective number of optical modes we can reliably measure for the backscattering light (reduced from the actual number of optical modes due to wave front measurement error) divided by the number of optical modes in the ultrasound spot (M_{US}). The relationship is derived in Section 2.3.3.

2.3.1 Photon budget calculation

We used the diffusion approximation to calculate light propagation in scattering biological tissue. For simplicity, we used the light diffusion equation for a steady-state source, which is given by

$$\left(-D\nabla^2 + \mu_a\right)\Phi(\vec{r}) = q_0(\vec{r}) \quad (1)$$

where the diffusion constant D and source term $q_0(\vec{r})$ are defined by

$$D = \frac{1}{3(\mu_a + \mu'_s)}, \text{ and } q_0(\vec{r}) = \int_{4\pi} \epsilon(\vec{r}, \hat{s}) d\Omega = 4\pi\epsilon(\vec{r}).$$

$\Phi(\vec{r})$ is the fluence rate with units W/m^2 , μ_a and μ'_s are the absorption and reduced scattering coefficient, respectively, and $\epsilon(\vec{r}, \hat{s})$ is the amount of source power density generated along \hat{s} at the small solid angle $d\Omega$ which is in units W/m^3 . \vec{r} is a position vector. The coordinate system used in this analysis is described in Fig. 1 and Table 1. Because the light pulse ($p_{\text{dur}} = 10\text{ ns}$ long) is not significantly broadened, we simply use the source with the net power corresponding to the power of a single pulse ($= 20\text{ mJ cm}^{-2} \times 5.1\text{ cm}^2 / 10\text{ ns}$) and integrate for one pulse duration to get the photon fluence for each pulse. Equation (1) is derived from the radiative transfer equation with the assumption that the light radiance can be expressed as an isotropic fluence plus a small directional flux [22]. The assumption is generally valid when the light propagation is scattering-dominated, and the position under consideration is far enough from the source ($> 1/\mu'_s$).

Then, the solution for steady-state Dirac-Delta source ($q_0(\vec{r}) = \delta^3(\vec{r})$) at the origin is simply

$$\Phi_{\text{point}}(\vec{r}) = \frac{1}{4\pi r D} e^{-\mu_{\text{eff}} r} \quad (2)$$

where $\mu_{\text{eff}} = \sqrt{\mu_a/D}$ is the effective attenuation coefficient. To get the fluence for the collimated incident beam hitting the semi-infinite medium, we approximated the incident beam with 0.2 mm -spaced point sources at the depth of transport mean free path ($1/\mu'_s$)

where the photon loses its directionality (pencil beam approximation) [22]. We used a zero-boundary condition to take into account the effect of the boundary [23]. That is,

$$\begin{aligned}\Phi(\vec{r}) &= \Phi(x, y, z) \\ &= \sum_{i \in \text{point sources}} \frac{P_{\text{point}}}{4\pi |\vec{r} - (x_i, y_i, 1/\mu'_s)| D} e^{-\mu_{\text{eff}} |\vec{r} - (x_i, y_i, 1/\mu'_s)|} \\ &\quad - \frac{P_{\text{point}}}{4\pi |\vec{r} - (x_i, y_i, -1/\mu'_s)| D} e^{-\mu_{\text{eff}} |\vec{r} - (x_i, y_i, -1/\mu'_s)|}\end{aligned}\quad (3)$$

where the P_{point} is the power of each point source, $E_{\text{point}}/p_{\text{dur}} \cdot E_{\text{point}}$ is the energy of each light pulse each point source is sampling ($20 \text{ mJcm}^{-2} \times (0.2 \text{ mm})^2$). The fluence can be interpreted as the number rate of photons passing through a certain point, with units of photon number/($\text{mm}^2 \cdot \text{sec}$). Thus, we estimate the number of photons passing through the ultrasound spot (N_{USP}) per pulse by multiplying the fluence by the area of the ultrasound focal spot and pulse duration. That is,

$$N_{\text{USP}} = \Phi(\vec{r}_{\text{US}}) \times A_{\text{US}} \times p_{\text{dur}} / (hc/\lambda) \quad (4)$$

where $\vec{r}_{\text{US}} = (0, 0, d_{\text{US}})$ is a position vector of the US spot, d_{US} is the depth of the US spot, $A_{\text{US}} = \pi \lambda_{\text{US}}^2 / 2$ is the surface area of the US spot, and λ_{US} is the ultrasound wave length. We assumed that the US spot is ellipsoidal with transverse and axial sizes of $\lambda_{\text{US}}/2$ and λ_{US} , respectively.

There are two main mechanisms of ultrasonic light modulation – the displacement of scatterers and the change in refractive index induced from ultrasonic pressure [6]. The modulation contributed from the moving scatterers is negligible compared to that from ultrasound-driven index grating, because the number of scattering events is low due to the small US spot size. Thus, we modeled the ultrasound spot as the refractive index grating with the amplitude

$$\Delta n = \frac{\partial n}{\partial p} P \quad (5)$$

where $\partial n / \partial p$ is a piezo-optic coefficient of the medium. We used the piezo-optic coefficient for water, $1.466 \times 10^{-10} \text{ Pa}^{-1}$ [24]. These parameters satisfy the following standard to use the Raman-Nath theory for nearly all incidence angles of light [25,26]:

$$\frac{Q'(\theta)\tau(\theta)}{2} \leq 1 \quad (6)$$

where the parameter $Q'(\theta)$ is $2\pi\lambda l / n_0 \lambda_{\text{US}} \cos \theta$, $\tau(\theta) = \pi \Delta n l / \lambda \cos \theta$ is the modulation parameter, and l is the light-sound interaction length. This condition is satisfied up to $\sim 88^\circ$ ($\equiv \theta_{\text{max}}$) with $\lambda_{\text{US}} = 30 \mu\text{m}$. The effective light-ultrasound interaction length was estimated as $\lambda_{\text{US}}/2$ based on the NA ($=1$) of the ultrasound transducer. Then, from the Raman-Nath theory, the first-order diffraction efficiency is simply given by

$$\eta(\theta) = J_1^2(\tau(\theta)) \quad (7)$$

[25–27]. Then, the ultrasound-modulated photon number per pulse can be calculated as

$$N_{USM} = \left(N_{USP} \int_0^{\theta_{\max}} \eta(\theta) d\theta \right) / \theta_{\max} \quad (8)$$

because θ_{\max} (incidence angle where the Raman-Nath theory is valid up to) is near 90° and irradiance is nearly isotropic in the diffusive regime.

As the last step of light propagation simulation, we calculate the propagation of the tagged photons to the tissue surface. We first assume the point source matched with the light power calculated from the previous step. As with the simulation of incident light propagation, diffusion approximation with a zero-boundary condition is used to calculate the flux (with units W/m^2) from the tissue surface, which is given by

$$\begin{aligned} \bar{J}(\vec{r}) &= -D\nabla\Phi(\vec{r}) \\ &= \frac{\Phi(\vec{r}_{US})A_{US}\eta}{4\pi|\vec{r}-\vec{r}_{US}|^2} \left(\frac{1}{|\vec{r}-\vec{r}_{US}|} + \mu_{\text{eff}} \right) e^{-\mu_{\text{eff}}|\vec{r}-\vec{r}_{US}|} (\vec{r}-\vec{r}_{US}) \\ &\quad - \frac{\Phi(\vec{r}_{US})A_{US}\eta}{4\pi|\vec{r}+\vec{r}_{US}|^2} \left(\frac{1}{|\vec{r}+\vec{r}_{US}|} + \mu_{\text{eff}} \right) e^{-\mu_{\text{eff}}|\vec{r}+\vec{r}_{US}|} (\vec{r}+\vec{r}_{US}) \end{aligned} \quad (9)$$

where η is angle-averaged modulation efficiency ($= \int_0^{\theta_{\max}} \eta(\theta) d\theta / \theta_{\max}$) [2,22]. The flux map was evaluated for every 0.1 mm over the $20\text{ cm} \times 20\text{ cm}$ area on which the OPC plane is assumed to be present. Because the speckle size is $\lambda/2$, the flux map is converted to the map of the average number of signal photons per mode (speckle) at each grid cell ($N_{\text{mode}}(x_{l,m}, y_{l,m})$) using the following relationship (l, m are indices for grid cells)

$$N_{\text{mode}}(x_{l,m}, y_{l,m}) = J_z(x_{l,m}, y_{l,m}) \times (\lambda/2)^2 \times p_{\text{dur}} / (hc/\lambda). \quad (10)$$

where $J_z(x_{l,m}, y_{l,m})$ is flux along z-axis. Then, by calculating wavefront measurement error induced from the shot noise at the signal level ($N_{\text{mode}}(x_{l,m}, y_{l,m})$), we estimated contrast (PBR) of TRUE focal spot. The detailed method will be described in Section 2.3.2 and 2.3.3.

2.3.2 Phase measurement error calculation

Before estimating the theoretical PBR from the flux map, we first investigate the phase measurement error of the 4-step phase-shifting method while assuming only Poissonian shot noise. In the 4-step phase-shifting method [14], the intensity of each interference is expressed by

$$\begin{aligned} I_i &= |E_{\text{ref}} + E_{\text{sig}} + E_{\text{unmod}}|^2 \\ &= A_{\text{ref}}^2 + A_{\text{sig}}^2 + A_{\text{unmod}}^2 + 2A_{\text{ref}}A_{\text{sig}}\cos(\phi_{\text{ref}_i} - \phi_{\text{sig}}) \\ &\quad + 2A_{\text{ref}}A_{\text{unmod}}\cos(\phi_{\text{ref}_i} - \phi_{\text{unmod}}) + 2A_{\text{sig}}A_{\text{unmod}}\cos(\phi_{\text{sig}} - \phi_{\text{unmod}}) \end{aligned} \quad (11)$$

where $E_{\text{ref}} = A_{\text{ref}}e^{i\phi_{\text{ref}}}$ is a reference field (frequency-shifted), $E_{\text{sig}} = A_{\text{sig}}e^{i\phi_{\text{sig}}}$ is a signal field (frequency-shifted), $E_{\text{unmod}} = A_{\text{unmod}}e^{i\phi_{\text{unmod}}}$ is a unmodulated light field, and A and ϕ represent amplitude and phase, respectively. As only $2A_{\text{ref}}A_{\text{sig}}\cos(\phi_{\text{ref}_i} - \phi_{\text{sig}})$ term serves as signal term, the signal-to-noise (Poissonian shot noise) ratio (SNR) can be defined by

$$SNR = \frac{2A_{ref}A_{sig}}{\sqrt{A_{ref}^2 + A_{unmod}^2 + A_{sig}^2 + 2A_{ref}A_{unmod} + 2A_{sig}A_{unmod}}} \frac{1}{\sqrt{hc/\lambda}} \quad (12)$$

where h is planck's constant. When the reference beam intensity is much larger than the others ($A_{ref}^2 \gg A_{sig}^2, A_{unmod}^2$), the SNR is maximized to $2A_{sig}/\sqrt{hc/\lambda}$ ($= 2\sqrt{\text{signal photon number}}$). We computed the phase from the four computationally generated interferograms with a large reference beam intensity and compared it with the actual phase. By repeating the procedure for many speckles, we could build the probability density function for the phase measurement error at different signal levels. For the creation of the interferogram, A_{sig} and ϕ_{sig} are randomly generated from Rayleigh distribution and uniform random distribution, respectively, based on the statistics of fully developed speckles. Then, the Poissonian shot noise with a standard deviation of $A_{ref}/\sqrt{hc/\lambda}$ ($= \sqrt{I_{ref}}/(hc/\lambda)$, generated with random number generator) is added to each interferogram. This exercise gives a better understanding on how the low signal intensity affects to the phase measurement error.

With this approach to determine wavefront measurement error, we calculated the field contribution from a single grid cell (M_{grid} number of modes) to the TRUE spot so that shot-noise-induced wavefront error was related with the reduction in OPC efficiency (reduction in effectively reliable number of optical modes). The PBR was then evaluated by summing up the field contribution from each simulation grid cell. This calculation is based on the time-reversal symmetry of the scattering process, which is described in the following section.

2.3.3 PBR calculation

Because scattering is a reciprocal process, we can expect scattering to possess time reversal symmetry. This property can be interpreted as following:

$$\begin{aligned} A_0 \text{ (input mode)} &\rightarrow A_k e^{i\phi_k} \text{ (} k_{th} \text{ mode measured at OPC plane)} \\ E_k \text{ (} k_{th} \text{ mode played back at OPC plane)} &\rightarrow \frac{A_k}{A_0} e^{i\phi_k} E_k \text{ (time-reversed input mode)} \end{aligned} \quad (13)$$

where A_0 is the incident signal light field on the input mode, $E_k = A_{ref}^{-i\psi_k}$ is a phase-conjugated light field displayed at the OPC plane (SLM surface), A_k and ϕ_k are amplitude and phase of each speckle. ϕ_k and ψ_k can be thought as the actual and measured (played-back) phases of each speckle. Thus, if we perform OPC for the single input mode and there is no wavefront measurement error ($\psi_k = \phi_k$, when the signal intensity is high enough), the resultant field at the time-reversed input mode can be expressed by the following equation

$$E_{OPC} = \sum_k^{M_{mode}} \frac{A_k e^{i\phi_k}}{A_0} E_k = \sum_k^{M_{mode}} \frac{A_k}{A_0} A_{ref} \quad (14)$$

where A_{ref} is the amplitude of the phase-conjugated light, and M_{mode} is the number of modes on OPC plane. Again, we assumed that the OPC system only modulates phase. We also note that speckle amplitude (A_k) follows Rayleigh statistics by neglecting all the correlation between speckles (the transmission matrix component mentioned in the Assumptions section). By assuming plane wave illumination ($\psi_k = 0$), the field at the background is expressed by

$$E_{Back} = \sum_k^{M_{mode}} \frac{A_k e^{i\phi_k}}{A_0} A_{Ref} \quad (15)$$

Then, by definition, PBR is [9,28]

$$PBR_{single} = \frac{\sum_k^{M_{mode}} E_{OPC} E_{OPC}^*}{\sum_k^{M_{mode}} E_{Back} E_{Back}^*} \approx \frac{\pi}{4} M_{mode} \quad (16)$$

When wavefront error resulting from shot-noise is present, the intensity at the OPC spot is reduced to

$$E_{OPC} E_{OPC}^* = \left| \sum_k^{M_{mode}} \frac{A_k e^{i\phi_k}}{A_0} A_{Ref} e^{-i\psi_k} \right|^2 \quad \text{with phase measurement error} \quad (17)$$

Because of the huge number of optical modes (2.5×10^{11} speckles), we cannot use a simple Monte-Carlo approach (speckle by speckle). Instead, the contribution from M_{grid} number of modes on each simulation grid cell is pre-calculated for different average photon numbers, with the shot noise-induced wavefront error (grid cell by grid cell). This leads to a lookup table (LUT) relating the shot noise to the reduction in OPC efficiency. Then, we evaluated the field at the OPC spot by interpolating/extrapolating (from LUT) and summing up the field contribution ($A_{OPC_LUT}(N_{mode}(x_{l,m}, y_{l,m})) e^{i\phi_{OPC_LUT}(N_{mode}(x_{l,m}, y_{l,m}))}$) from each simulation grid cell with the average signal photon number ($N_{mode}(x_{l,m}, y_{l,m})$). Mathematically, it is expressed as

$$\begin{aligned} E_{OPC} &= \sum_k^{M_{mode}} \frac{A_k}{A_0} A_{Ref} e^{i(\phi_k - \psi_k)} = \sum_{l,m}^{M_{grid}} \sum_{k \in cell_{l,m}} \frac{A_k}{A_0} A_{Ref} e^{i(\phi_k - \psi_k)} \\ &= \sum_{l,m} A_{OPC_LUT}(N_{mode}(x_{l,m}, y_{l,m})) e^{i\phi_{OPC_LUT}(N_{mode}(x_{l,m}, y_{l,m}))} \end{aligned} \quad (18)$$

where A_{OPC_LUT} and ϕ_{OPC_LUT} are the interpolation operators for amplitude and phase. The same approach has been used to calculate the background field assuming a plane phase map.

Equation (18) is for OPC procedure for single input mode. On the other hand, in the case of TRUE focusing, the number of input modes can be estimated by

$$M_{US} = \frac{2A_{US}}{(\lambda/2)^2} \quad (19)$$

where λ is the light wavelength. The factor of 2 is for considering modes propagating to either direction (with respect to the plane PBR is calculated on).

As the power of the OPC beam is distributed to the input modes, the PBR of the TRUE focal spot is given by

$$PBR_{TRUE} = \frac{\pi}{4} \frac{\sum_k^{M_{mode}} E_{OPC} E_{OPC}^*}{\sum_k^{M_{mode}} E_{Back} E_{Back}^*} \quad \text{with phase measurement error.} \quad (20)$$

Both E_{OPC} and E_{Back} are calculated as the sum of contributions from grid cells (A_{OPC_LUT} and A_{Back_LUT}). The number of physical optical modes across the OPC plane

($20\text{cm} \times 20\text{cm}$) is 2.5×10^{11} and the number of input modes at the ultrasound plane is $\sim 1.8 \times 10^4$ for 800nm . Thus, the ideal PBR_{TRUE} (without phase measurement error) is $\sim 1.4 \times 10^7$ for 800nm , regardless of the depth. However, as derived above, PBR_{TRUE} decreases with depth due to the error in wavefront measurement.

We note that by this characterization, PBR_{TRUE} has a scaling relationship with the physical number of optical modes, and the signal level, which can be simply calculated with diffusion approximation. As such, while we have generally chosen optical and ultrasonic parameters to reflect a general TRUE scenario, the PBR_{TRUE} found here can be easily rescaled by a reader interested in a different set of parameters.

2.3.4 Definitions of TRUE penetration depth limit

There are two ways we can define the penetration depth limits of TRUE from the simulation. Each is suitable for different applications. The primary way is to define TRUE depth limit ($depth_{local}$) as the depth at which PBR_{TRUE} decreases to the value of 2.

$$\text{1st standard : } PBR_{TRUE}(depth_{local}) = 2 \quad (21)$$

This standard essentially can be used to test the effectiveness of the TRUE focusing technique because PBR_{TRUE} is itself the contrast of the TRUE focus.

The second way is to define TRUE depth limit ($depth_{fluence}$) as the depth at which the photon fluence at the TRUE focus spot is at least higher than the incident light intensity at the sample's surface. The fluence at the TRUE focal spot can be simply calculated by

$$\Phi_{TRUE} = \Phi_{Back}(\vec{r}_{US}) \times PBR_{TRUE} \quad (22)$$

where $\Phi_{Back}(\vec{r}_{US})$ is the background light fluence, which can be simply calculated by assuming plane wave illumination with the desired playback light intensity ($I_{playback}$). In short, $\Phi(\vec{r}_{US})$ can be thought of as background fluence. Therefore, the second standard is

$$\text{2nd standard : } \frac{\Phi_{TRUE}(depth_{fluence})}{I_{playback}} = 1. \quad (23)$$

The first definition is more generally useful and characterizable, as it simply tests for the presence or absence of TRUE-guided light at the aimed TRUE focus location. This is the definition we use predominantly. On the other hand, the second condition ensures that more light power is delivered to the point in the TRUE focal spot than the point on the tissue surface. So, for instance, it would be a useful standard for applications requiring an absolute optical power, such as “optical burning”.

3. Results

The simulation results presented in this paper are aimed at predicting the key variables of TRUE focusing. Therefore the structure of the results section mirrors the physical TRUE focusing process.

For photon budget calculation, we note that all the plots are results from the 800nm light source, which leads to the largest penetration depth. First, Fig. 3(a) shows the photon fluence map of the incident probe light corresponding to a single pulse propagating through the tissue medium. Figure 3(b) shows the number of photons passing through the US spot (N_{USP}). Because a very small portion of the diffused photons pass through the ultrasound spot, there is

a significant loss in photon budget. For example, at the depth of ultrasound of 50 mm , only $\sim 1.1 \times 10^{11}$ photons pass through the ultrasound spot among the $\sim 2.1 \times 10^{18}$ number of incident photons for each pulse. Because, at 532 nm and 633 nm , the light source is more scattered and absorbed, a smaller portion of photons hit the ultrasound spot.

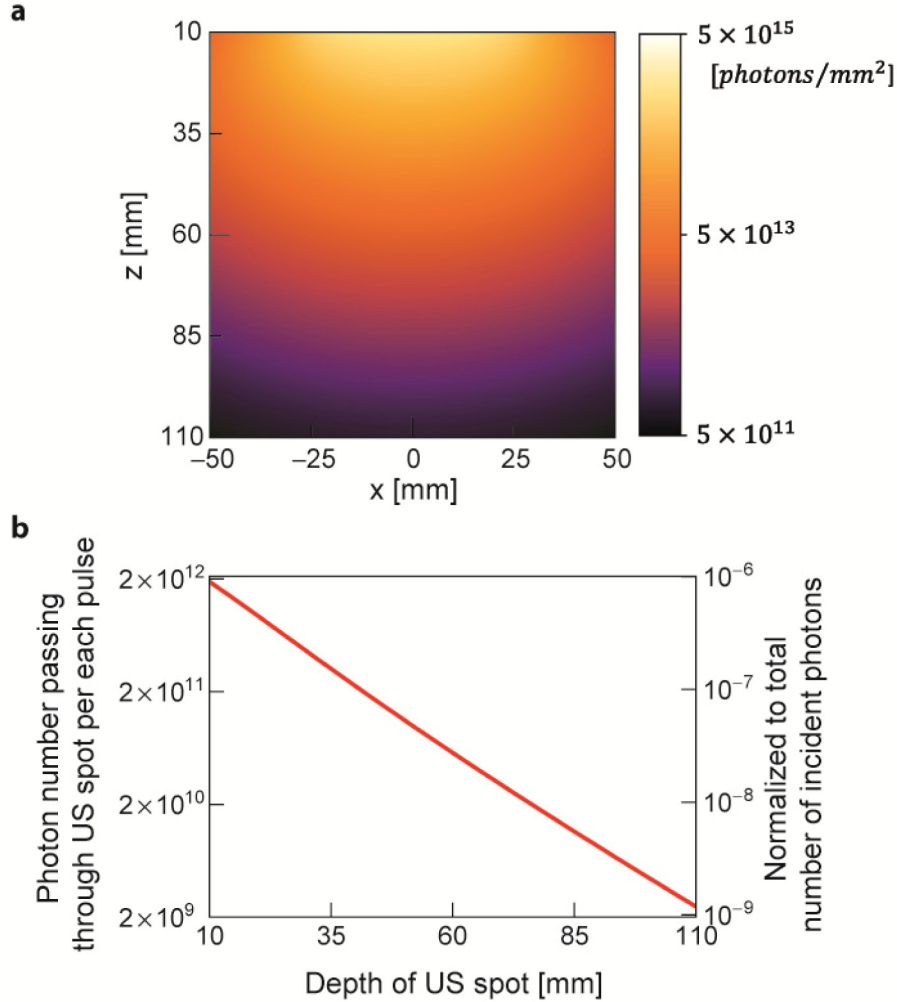


Fig. 3. (a) Longitudinal sectional photon fluence map of the light beam propagating through the biological tissue corresponding to a single light pulse at the safety limit. The map is plotted in log scale. The wavelength is 800 nm . We calculated the number of photons passing through the US spot ($\Phi(r_{US}) \times p_{dur} / (hc/\lambda)$) by multiplying the photon flux at target depth with the longitudinal cross-sectional area of US spot. (b) Number of photons passing through the US spot is plotted along depth. The scale on the right axis represents the corresponding photon numbers normalized by the number of incident photons. The plot is in log scale.

Then, the photons passing through the US spot are ultrasonically modulated by the efficiency depending on the incident angle of the light to the thin refractive index grating that is generated from the ultrasonic pressure (Fig. 4). We averaged the efficiency given by

Raman-Nath theory up to θ_{\max} ($\eta = \int_0^{\theta_{\max}} \eta(\theta) d\theta / \theta_{\max}$). This results in a modulation efficiency of ~ 0.0067 . For 532 nm and 633 nm , the efficiencies are ~ 0.013 and ~ 0.010 , respectively.

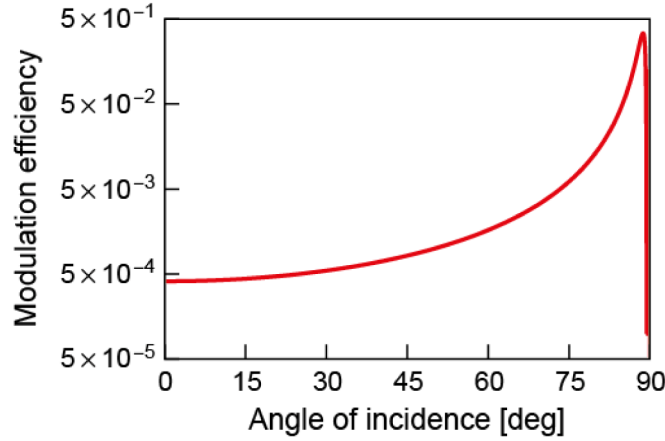


Fig. 4. Dependence of ultrasonic modulation efficiency ($\eta(\theta)$) on the incident light angle as calculated by the Raman-Nath theory for an 800 nm light source and an ultrasonic pressure of 2.35 MPa . As $\theta_{\max} (\simeq 88^\circ)$ is around 90° and the light irradiance is nearly isotropic in the diffusing regime, we averaged out the modulation efficiency for incidence angles of $[0, \theta_{\max}]$. This results in a value of ~ 0.0067 (for 532 nm and 633 nm , ~ 0.013 and ~ 0.010 , respectively). The number of modulated photon numbers (N_{USM}) is calculated by multiplying the averaged modulation efficiency with the number of photons passing through the US spot (N_{USP}). The plot is in log scale.

Following this, we propagate the modulated light back to the tissue surface. Figure 5(a) shows the average number of photons emerging from each speckle ($N_{\text{mode}}(x_{l,m}, y_{l,m})$) for a single interferogram (corresponding to a single pulse) when the ultrasound spot is at a depth of 50 mm . We note that the photon number per speckle drops to much lower than 1, and will show that TRUE focusing can be achieved even with this photon budget. Figure 5(b) shows the total number of photons emerging from the surface. Because most back-scattered light falls into the region of the $20\text{ cm} \times 20\text{ cm}$ simulation grid, the photon budget loss is less significant than that in the first step. For example, for the depth of ultrasound of 50 mm , $\sim 5.7 \times 10^7$ photons emerge from the surface among $\sim 7.5 \times 10^8$ modulated photons at the US spot per pulse. Because of the same reason as in incident light propagation, a smaller portion of photons can be detected with 532 nm and 633 nm .

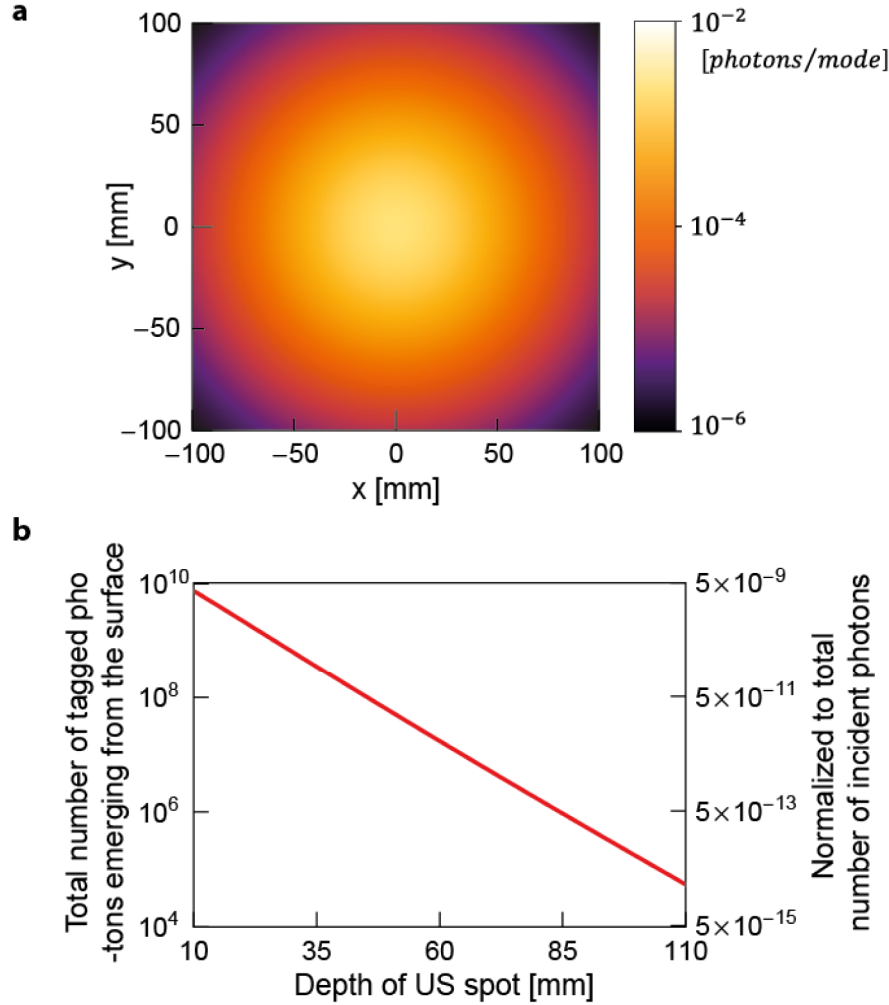


Fig. 5. (a) 2D photon flux map of ultrasonically modulated light emerging from the tissue surface from a single incident light pulse. The map is plotted in log scale. The target depth is 5 cm and the wavelength is 800 nm . We calculated the average number of photons per mode ($N_{\text{mode}}(x_{l,m}, y_{l,m})$) by dividing the photon flux at each grid cell ($J(x_{l,m}, y_{l,m})$) by the number of modes inside each grid cell (M_{grid}). (b) The total number of emerging photons at the surface is plotted for various depths. The scale on the right axis represents corresponding photon numbers normalized by the number of incident photons. The plot is in log scale.

Before evaluating the PBR from the photon flux map, we investigated the effect of shot noise on the phase measurement error of individual optical modes at different average signal photon numbers ($I_{\text{sig}}/(hc/\lambda) = A_{\text{sig}}^2/(hc/\lambda)$) (Fig. 6). We note that the SNR is $2A_{\text{sig}}/\sqrt{hc/\lambda}$ as derived in Section 2.3.2 with an assumption of large reference beam intensity ($A_{\text{ref}}^2 \gg A_{\text{sig}}^2, A_{\text{unmod}}^2$). The phase error distribution becomes uniform as the number of signal photons is decreased. However, the PDF shows the slight confinement around 0 even with a signal photon number of 0.01. This implies that the measured phase is more likely in the same direction with correct phase in complex plane. This tendency results in a partially constructive interference (of different optical modes at DOPC plane) at OPC spot (TRUE focal spot) even

in circumstances in which the emerging photon per speckle ($N_{\text{mode}}(x_{l,m}, y_{l,m})$) is much lower than 1.

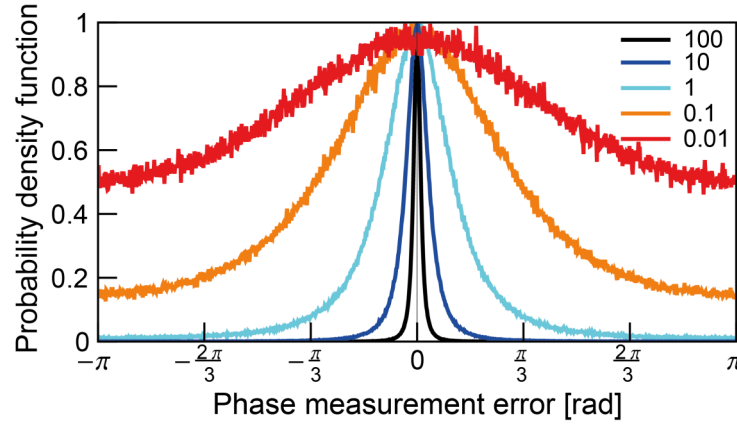


Fig. 6. Normalized probability density function of the phase measurement error at different average signal level ($I_{\text{sig}} / (hc/\lambda) = A_{\text{sig}}^2 / (hc/\lambda) - 100, 10, 1, 0.1, 0.01$ photon(s). The

PDF is built with the Monte-Carlo simulation of 4 step phase shifting method for 10^5 number of modes. The error is increased as the signal is decreased. Though it is wide, peak around 0 is observed even at signal photon number smaller than 1.

Then, we build the relationship of PBR degradation with the wavefront measurement error. As mentioned above, we utilize the grid cell-wise field contribution (from the DOPC plane to the TRUE spot) which is prebuilt in LUT. More specifically, the LUT relates the average signal photon number per mode ($N_{\text{mode}}(x_{l,m}, y_{l,m})$) with the field contribution $A_{\text{OPC_LUT}}$ and $\phi_{\text{OPC_LUT}}$ (from a single simulation grid cell consisting of M_{grid} number of modes). Figure 7(a) shows the intensity contribution (square of amplitude, $A_{\text{OPC_LUT}}^2$) from a single grid cell when phase conjugation is performed for the single input mode. The plot is normalized with the ideal intensity in the case without wavefront measurement error. The intensity contribution is not degraded significantly with more than 10 photons per mode (on average). However, shot noise at a low signal limit dramatically deteriorates the intensity contribution. For the sake of comparison with the background ($A_{\text{Back_LUT}}^2$), Fig. 7(b) shows the PBR of the OPC spot optimizing a single input. PBR decreases to 1 at a low signal photon limit and saturates to the theoretically expected value, $\pi M_{\text{grid}} / 4 (= 4.9 \times 10^4)$, with sufficient photon budget to precisely characterize the wavefront. Insets present the resultant phase of the phase-conjugated field ($\phi_{\text{OPC_LUT}}$) at different signal photon levels. As the PBR closes to 1 at the low photon budget limit, the resultant phase ($\phi_{\text{OPC_LUT}}$) of the phase-conjugated field becomes uniform (Fig. 7(b) insets). In spite of the degradation, the PBR is still well above 1 even when the photon budget per speckle is, on average, only 10^{-4} . From the LUTs, OPC and background field contributions ($A_{\text{OPC_LUT}}$, $A_{\text{Back_LUT}}$, and $\phi_{\text{OPC_LUT}}$) from each grid cell is interpolated (at simulated signal photon number, $N_{\text{mode}}(x_{l,m}, y_{l,m})$). Then, by summing up and squaring the field contributions for OPC peak and background field, respectively, peak intensity (single mode) and background intensity is calculated. It gives the PBR_{single} (with phase measurement error). PBR_{TRUE} is simply $PBR_{\text{single}} / M_{\text{US}}$.

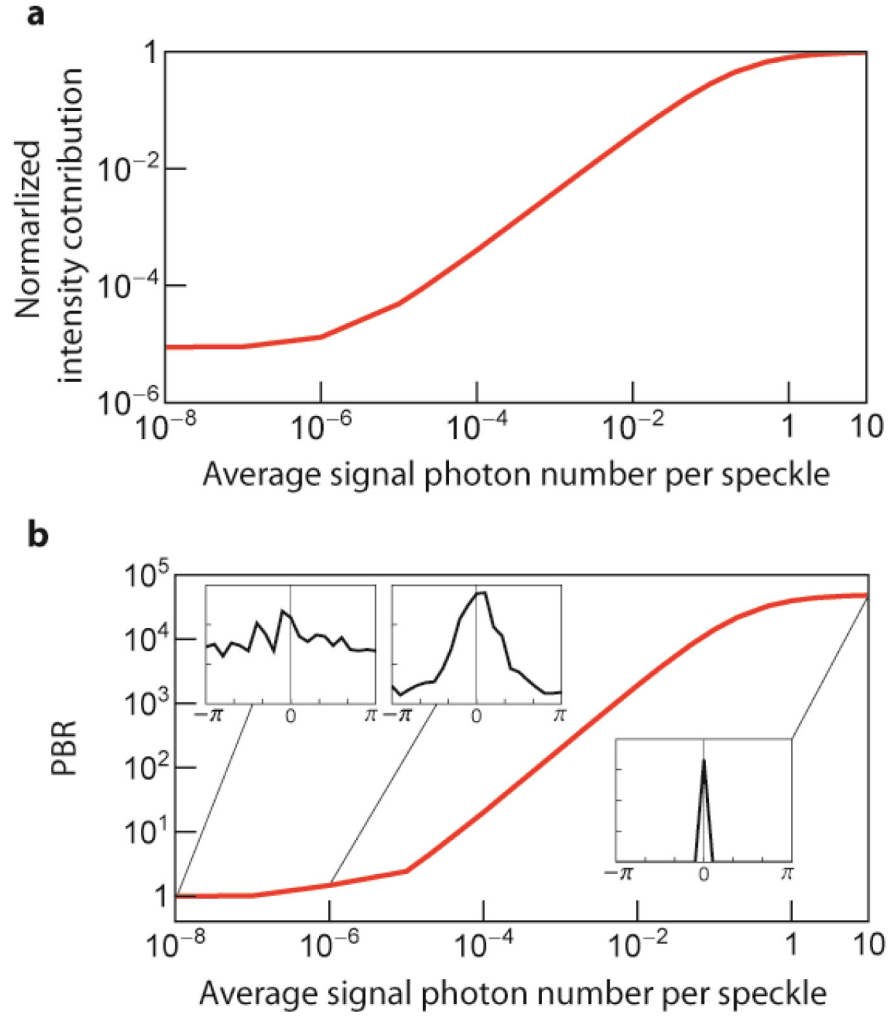


Fig. 7. (a) Normalized intensity contribution from the single grid cell ($0.1\text{ mm} \times 0.1\text{ mm}$) to a single input mode ($A_{OPC_LUT}^2$) when OPC is performed for $M_{grid} (= 6.25 \times 10^4)$ number of modes. The plot is normalized with the ideal intensity contribution in the case without wavefront measurement error which has a linear dependence on the average signal photon number. As the average signal photon number decreases, the wavefront measurement error across M_{grid} number of modes increases, resulting in a dramatic reduction in intensity contribution. (b) Dependence of PBR on the average signal photon number when OPC is performed on single grid cell for the single input mode. By assuming plane wave front, background intensity contribution is calculated. Then, PBR is calculated by dividing peak intensity contribution with the background intensity contribution. PBR drops to 1 at low signal photon limit and saturates to $\pi M_{grid}/4 (= 4.9 \times 10^4)$ when there is enough signal photon for an accurate phase measurement. The insets show the resultant phase distribution (PDF) of the phase-conjugated field (ϕ_{OPC_LUT}) at different signal photon level. The plots are in log-log scale.

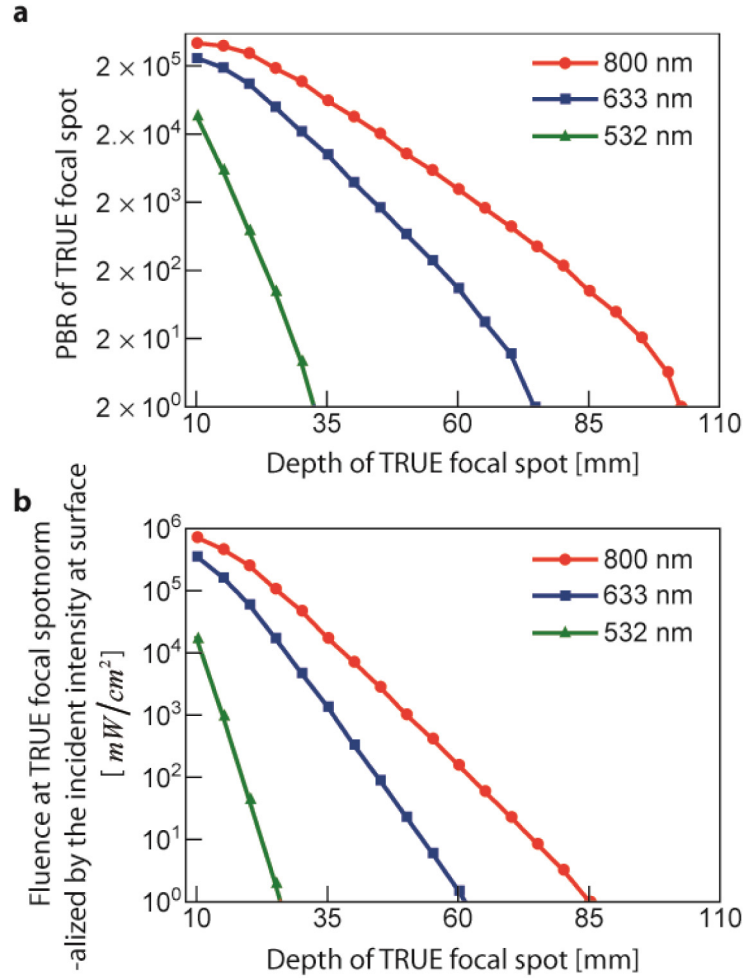


Fig. 8. (a) Dependence of PBR of TRUE focal spot on the target depth. Penetration depth limit is $\sim 103\text{ mm}$ ($depth_{local}$ where $PBR_{TRUE} = 2$) with 800 nm (red line, circle marker). (b) Dependence of fluence at TRUE focal spot normalized by the incident playback light intensity at surface. Light power on the TRUE focal spot becomes weaker than the incident light power from $\sim 85\text{ mm}$ ($depth_{fluence}$) for 800 nm . Penetration depth limits for both standards are reduced to $\sim 34\text{ mm}$ and $\sim 75\text{ mm}$ ($depth_{local}$), $\sim 25\text{ mm}$ and $\sim 62\text{ mm}$ ($depth_{fluence}$), for 532 nm (green line, triangle marker) and 633 nm (blue line, square marker) light, respectively. The plots are in log scale.

Figure 8(a) shows the dependence of PBR_{TRUE} on the depth of the target spot. The PBR nearly exponentially drops as the depth increases. We determined the two penetration depth limits ($depth_{local}$, $depth_{fluence}$), respectively. Based on the first standard ($PBR_{TRUE} \geq 2$), the TRUE focal spot can be created at up to $\sim 103\text{ mm}$ ($depth_{local}$). For the 532 nm and 633 nm light sources, $depth_{local}$ is reduced to $\sim 34\text{ mm}$ and $\sim 75\text{ mm}$, respectively. For the second standard, Fig. 8(b) presents the fluence at the target spot (Φ_{TRUE}) normalized by the incident light intensity. Even though the TRUE focal spot can be created (peak contrast $PBR_{TRUE} \geq 2$),

light (Φ_{TRUE}) is actually not more concentrated at TRUE focal spot compared to the incident light intensity of the phase-conjugated beam at the tissue surface for depths over $\sim 85\text{mm}$ ($depth_{fluence}$). The second condition for $depth_{fluence}$ is generally more restrictive than the first standard for $depth_{local}$. The PBR_{TRUE} is around 100 at $depth_{fluence}$ with the parameters in our consideration. $depth_{fluence}$ is decreased to $\sim 25\text{mm}$ and $\sim 62\text{mm}$ for 532nm and 633nm , respectively.

4. Discussion

In this study, we have developed a computational method to track the photon budget during the TRUE focusing process and investigate the fundamental limit in the penetration depth of the TRUE focusing technique.

As expected, the photon budget is decimated during light propagation from the tissue surface to the US spot, because the US spot is much smaller than the region covered by the diffuse light. We also found that an idealized OPC procedure can reconstruct the time-reversed focus even when the average photon number per mode is smaller than 1. At the low photon budget limit, the distribution of phase measurement error significantly spreads out to a large value. However, there still is a slight tendency for the error distribution to peak around 0. So, when the number of phase-conjugated modes is large, this subtle tendency results in the partially coherent addition of the OPC field from each optical mode on the DOPC plane.

We determined two penetration depth limits of TRUE focusing technique ($depth_{local}$, $depth_{fluence}$) from two separate standards: the PBR should be higher than 2, and the photon fluence at the TRUE spot should be higher than the incident light intensity on the surface so that more light is actually delivered to the spot. For an 800nm light source, a 50MHz ultrasound frequency, and a 2.35MPa ultrasonic pressure at the US spot, and with typical optical properties for chicken tissue (reduced scattering coefficient ($\mu'_s = 0.17\text{mm}^{-1}$), absorption coefficient, $\mu_a = 0.005\text{mm}^{-1}$) the TRUE focusing technique can create focus up to $\sim 103\text{mm}$ ($depth_{local}$). In terms of power delivery ($\Phi_{TRUE}(depth_{fluence}) = I_{\text{playback}}$ at the surface), the TRUE focusing technique is effective up to $\sim 85\text{mm}$ ($depth_{fluence}$). As 532nm and 633nm light sources are more scattering and the light is absorbed through the biological tissue, the penetration depths are reduced to $\sim 34\text{mm}$ and $\sim 75\text{mm}$ ($depth_{local}$), and $\sim 25\text{mm}$ and $\sim 62\text{mm}$ ($depth_{fluence}$), respectively.

The result will vary depending on the parameters used in the numerical model. For instance, we performed the simulation for 10MHz ultrasound frequency, as the ultrasound of 50MHz is expected to be attenuated dramatically ($0.54\text{dB MHz}^{-1}\text{cm}^{-1}$ for soft tissue) [29]. First, more photons pass through the US spot as the spot becomes larger with lower frequency. Then, more photons can be collected during wavefront measurement, and this results in a higher number of reliable optical modes on the DOPC plane. Thus, even though the optimized power is distributed to a larger number of optical modes at the US spot (M_{mode}), the PBR_{TRUE} is enhanced. The depth limits are calculated as $\sim 139\text{mm}$ and $\sim 100\text{mm}$ for $depth_{local}$ and $depth_{fluence}$, respectively (an 800nm light source is assumed). We can conduct further analyses on other parameters (light wavelength, incident light power, beam width of incident light, ultrasound pressure, physical size of the DOPC system) and it would be useful to find optimal parameters for different configurations. Moreover, it might be interesting to see how the penetration depth changes for different types of tissue.

Though we used the diffusion approximation with a zero-boundary condition for the simplicity, a more accurate method to simulate light propagation simulation (such as a numerical solution of RTE, the Monte-Carlo method) can be used. It also would be worthwhile to develop our model to simulate a more realistic case with a practical design such as finite well depth and finite sensitivity of the sensor, and a large pixel size for the DOPC system.

Acknowledgments

We thank Mr. Roarke Horstmeyer for helpful discussions. This work is supported by NIH 1DP2OD007307-01. Benjamin Judkewitz is recipient of a Sir Henry Wellcome Fellowship from the Wellcome Trust.